J Mater Sci

Electronic materials

Structural and phonon properties of CdTe thin films synthesized by discrete thermal evaporation

M. S. Tivanov[1,*], A A. Zgliui[1], V. A. Gevorgyan[2], O. V. Korolik[1], E. A. Kolesov[1], K. P. Haroyan[3], D. V. Zhyhulin[4], and V. F. Gremenok[5]

[1] *Faculty of Physics, Belarusian State University, 220030 Minsk, Belarus*
[2] *Scientific Laboratory of Thin-Film Structures and Nano-Composite Materials, Institute of Engineering and Physics, Russian-Armenian University, 0051 Yerevan, Armenia*
[3] *Nuclear and Radiation Safety Center, 0010 Yerevan, Armenia*
[4] *"Belmicroanalysis" State Center, "INTEGRAL" JSC - Holding Managing Company, Minsk, Belarus*
[5] *SSPA "Scientific-Practical Materials Research Centre of NAS of Belarus", 220072 Minsk, Belarus*

Received: 24 July 2025
Accepted: 12 September 2025

ABSTRACT

Despite the technological significance of CdTe, the influence of high-order phonon anharmonicity on phonon transport in thin films synthesized by discrete evaporation has not been sufficiently studied. This study investigates the temperature-dependent anharmonic phonon interactions in CdTe thin films synthesized by discrete thermal evaporation, to provide the basis of optimizing the thermo- and electrophysical properties of the material for use in high-performance photovoltaic and optoelectronic devices. The films, annealed in air at 400 °C, exhibited a cubic structure with near-stoichiometric composition (Cd/Te ≈ 1.1) and a grain size of ~ 1 μm. Temperature-dependent study analyzed the shifts and broadening of TO, LO, and 2LO phonon modes. Using the improved Klemens model, the contributions of thermal expansion as well as 3- and 4-phonon scattering were decoupled, revealing their distinct roles in phonon energy. Key findings include a nonlinear temperature dependence of phonon peak positions, with TO, LO, and 2LO modes shifting by 4.1, 5.6, and 10.7 cm^{-1}, respectively, upon cooling to 40 K; dominance of 3-phonon scattering below 200 K, while 4-phonon interactions prevailed at higher temperatures, contributing to the shift up to 7.6 cm^{-1} for 2LO modes; and dominance of 3-phonon process contribution to phonon linewidth broadening below 105 K, whereupon the contribution of 4-phonon scattering became the main process responsible for the broadening. The demonstrated synthesis method yields films with structural and compositional suitability for high-efficiency solar cells, while the analysis of temperature-dependent Raman results highlights the critical role of high-order lattice anharmonicity in CdTe, providing a foundation for optimizing CdTe-based devices.

Handling Editor: Kevin Jones.

Address correspondence to E-mail: michael.tivanov@gmail.com

https://doi.org/10.1007/s10853-025-11547-5

Springer

Introduction

Nowadays, CdTe is one of the well-studied materials used in photovoltaics and optoelectronics, since its research began about 60 years ago and continues to this day [1, 2]. CdTe has the zinc blende structure and belongs to the $A^{II}B^{VI}$ compounds [3]. It is a semiconductor material with the optimum for photoconversion band gap ($E_g = 1.5$ eV for the monocrystalline form and $E_g = 1.42$ eV for the polycrystalline form) [2] and the high optical absorption coefficient (α) near the absorption edge of about 10^5 cm^{-1} [4]. Also CdTe is chemically stable and strong. The achieved maximum photoconversion efficiency is 22.1% (the theoretical Shockley–Queisser limit is 32%) [1, 5]. Currently, CdTe thin films represent about 10% of the global photovoltaic technology [6].

The most common defects that can be formed in CdTe thin films are vacancies V_{Cd} and V_{Te}, interstitial defects Cd_i and Te_i, antisites Cd_{Te} and Te_{Cd}, etc. [7, 8]. It is known that a large number of structural defects, which contribute to the recombination of electron–hole pairs by impeding the movement of charge carriers, can be reduced by annealing CdTe thin films in a chlorine atmosphere. The annealing temperature is in the range of 350–400 °C. After such treatment, the appearance of a higher crystalline structure, change in morphology, disappearance of small grains, etc., are observed [9].

To study crystal sizes and orientation, deformation states and thermal properties, Raman spectroscopy is often used to directly characterize the phonon properties of the materials under study. For these purposes, the shift of the observed Raman bands is usually measured [10]. Raman analysis is characterized by good sensitivity to various material changes, convenience and, importantly, it is a nondestructive method [11].

Temperature-dependent Raman spectroscopy is an abundant source of experimental data regarding the anharmonic phonon properties of materials [12–19]. Since it enables one to obtain information on the phonon energy change under the heating (cooling) conditions—it can be applied to calculate anharmonic constants for phonon energy (peak position) and decay (linewidth) [13–18], as well as the extrapolated energy and decay at temperature close to absolute zero, which should be fundamentally determined by crystal structure of the material [20]. Phonon anharmonicity in principle will affect not only the phonon transport, but also the electronic transport as well through influencing the electron–phonon scattering rate [21, 22]. Furtherly, optimization of light absorption in thin-film devices, for example using toroidal multilayer structures [23], requires accurate consideration of optical phonon interactions. The data on optical mode anharmonicity then would provide parameters for the design of such structures based on CdTe. Thus, investigating anharmonic phonon–phonon interactions provides data useful for heat transport analysis, electric and thermoelectric properties of the material, as well as its advanced applications.

A wide range of methods exists for the deposition of high-quality functional films, where precise control over synthesis parameters is crucial for tailoring their microstructure and properties [24–27], among which are liquid phase deposition, molecular beam epitaxy (MBE), vacuum deposition, close-space sublimation (CSS), close-spaced vapor transport (CSVT), sputtering, spray pyrolysis and many others. In this work, CdTe thin films were synthesized by the discrete vacuum thermal evaporation method (a modified technique of the vacuum thermal evaporation method), which allows taking into account the difference between the partial pressures of the constituent elements in the obtained thin films. This enables one to produce samples with high degree of crystallinity and composition with strict stoichiometry [28, 29]. The development of CdTe-based technologies is not limited to pure films. Furthermore, the integration of CdTe semiconductor with carbon nanoforms (e.g., graphene, carbon nanotubes) presents a promising route for developing advanced composite materials with enhanced functional properties for optoelectronics and photovoltaics [30–32]. Thus, a fundamental understanding of the intrinsic properties of high-quality CdTe films, such as their phonon behavior and anharmonicity, becomes a crucial prerequisite for the effective engineering and performance optimization of such complex heterostructures [33].

The purpose of this work is to study the effect of temperature on anharmonic phonon processes in CdTe thin films, obtained by discrete thermal evaporation, using temperature-dependent Raman spectroscopy in the range from 40 to 295 K, and to determine the 3- and 4-phonon anharmonic constants for the TO, LO and 2LO modes, to provide the basis of optimizing the thermo- and electrophysical properties of the material for use in high-performance photovoltaic and optoelectronic devices. Although the temperature dependence of phonons in bulk CdTe has already been studied [16–18], such data are lacking for films obtained by discrete thermal evaporation. Since the controlled precursor feed minimizes the stoichiometric deviations, the phonon scattering by defects will be potentially reduced. This allows isolating the contribution of anharmonicity to temperature shifts, which was not achieved in previous studies.

In contrast to [16, 18], where 4-phonon effects in bulk CdTe were not taken into account, to studies focusing on first-principle simulation rather than calculating anharmonic constants [17], as well as to the work on CdS [19], which presented the total phonon shift without discerning different contributions, the present analysis clearly demonstrates the domination of 4-phonon interactions with the temperature increase. This indicates the need to take into account higher-order anharmonicity in devices operating near room temperature.

Methods

Preparation of CdTe thin films

CdTe thin films were deposited on glass substrate with the temperature of 270 °C by the discrete vacuum thermal evaporation. The temperature was chosen to ensure adhesion and crystallinity, reduce strain of the film and at the same time to prevent re-evaporation of Cd and Te during CdTe evaporation [34]. The glass substrate was previously cleaned using an ultrasonic bath. CdTe single crystal was used as a precursor material [35]. CdTe milled to powder with a particle size of 100–150 μm was fed from a vertically placed vessel into a molybdenum evaporation boat through an automatically controlled vibrating outlet. Adjustment of the rate of powder flow into the evaporation boat was possible due to the ability to open this outlet for times ranging from 0.2 to 0.5 s. The distance between the substrate and the molybdenum boat was about 12 cm, the base pressure was about 2×10^{-3} Pa, and the temperature of the evaporation boat was about 600–650 °C [29, 35]. A schematic of the evaporation device used to synthesize CdTe films is presented in [29].

CdTe thin films were annealed in air atmosphere at 400 °C for 1 h. The annealing temperature was chosen to promote recrystallization, as well as to reduce phonon scattering by point defects, in order to highlight anharmonic processes as the dominant mechanism of Raman peak broadening. Annealing at temperatures around 400 °C improves crystallinity, does not lead to the formation of secondary oxide phase components and relieves internal stresses.

Characterization details

X-ray energy-dispersive spectroscopy (EDX) and scanning electron microscopy (SEM) were performed using the S-4800 device (Hitachi). The secondary electron detection mode was used in order to investigate the surface morphology and cross-sections of CdTe films. The operating voltage was 7.2 kV for EDX and 7.0 kV for SEM.

Grazing incidence X-ray diffraction (GIXD) geometry at 1° of incident X-rays was applied to determine the phase composition and calculation of the structural parameters of thin films. GIXD analysis was performed by Ultima IV X-ray diffractometer in the scanning range from 10° to 80° (radiation source—CuKα, $\lambda = 0.15406$ nm).

To investigate the temperature dependences of the positions and FWHM of Raman bands, the Raman spectra were obtained in the temperature range from 40 to 295 K using Nanofinder HE (LOTIS TII) confocal Raman spectrometer. A solid-state laser with a wavelength of 532 nm and an optical power of ~ 0.2 mW was used for excitation Raman signal at room temperature in air (focusing spot on the film surface with a diameter of ~ 0.7 μm). During the low-temperature measurements, the samples were studied in a vacuum (less than 5×10^{-4} Pa, with a setting accuracy of ± 0.05 K) temperature-controlled cell. The laser spot diameter was of ~ 1.6 μm, optical power of ~ 1.6 mW. Exposition time for each spectrum was 30 s. Backscattered light was dispersed with 600 lines mm^{-1} diffraction grating with a spectral resolution better than 3 cm^{-1} (about 0.1 nm of the wavelength scale).

The laser radiation powers used (0.2 mW in air, 1.6 mW through the cell glass) were chosen to be close to the minimum detectable ones and were carefully optimized to obtain a reliable signal with the lowest possible impact on the sample in each configuration. The power of 0.2 mW in air is in the range where the heating of the bulk sample is generally recognized to be small. Increasing the power to 1.6 mW for measurements through the glass compensated for the significant light losses in the optical path of the cell, which is a standard practice for maintaining an adequate signal-to-noise ratio. A key confirmation of the adequacy of the chosen powers is the fact that the main Raman peaks of CdTe show identical positions and shapes in the spectra obtained in air and in the evacuated cell through the glass. The resulting laser power density was of 0.5 mW/µm^2 in air and of 0.8 mW/µm^2 in vacuum, which are below the threshold for nonlinear effects or significant heating in CdTe [18].

Results and discussion

Composition, surface and grazing incidence X-ray diffraction of CdTe thin films

The composition of elements in CdTe thin films was investigated by EDX spectroscopy. For the thin films under study, Cd and Te contents are 52.5 and 47.5 atomic percent, respectively. The stoichiometric ratio of Cd/Te is about 1.1.

The resulting SEM and cross-sectional images of investigated CdTe films (Fig. 1) show a homogeneous surface without voids. The grain sizes are of ~ 1 µm and larger. The thickness of CdTe thin film is 3.3 µm. Since the deposition time was 30 min, the average film growth rate was about 0.1 µm/min.

The received and theoretical GIXD patterns of CdTe thin films are shown in Fig. 2a. The observed peaks are in the 2Θ range from 20° to 80°. According to the theoretical data (ICSD Card No.: 01-070-804), the peaks at $2\Theta \approx 23.8°$, 39.3°, 46.4°, 62.4°, 71.2°, 76.3° are indicative of (111), (220), (311), (331), (422), (511) planes of the cubic crystal structure of CdTe.

The texture coefficient TC_{hkl} (Fig. 2b) was calculated based on the equation [36]:

$$TC_{hkl} = \frac{\frac{I(hkl)}{I_0(hkl)}}{\frac{1}{N}\sum_{i=1}^{N}\frac{I(h_ik_il_i)}{I_0(h_ik_il_i)}}, \tag{1}$$

where I_0 (hkl) is the theoretical peak intensity of the (hkl) plane of CdTe (according to the data in ICSD Card No.: 01-070-804), I(hkl) is the peak intensity of the plane (hkl) measured in this work, and N is a number of orientations taken into account in the calculation.

The findings indicate the preferable orientation along the (111) plane of the CdTe cubic structure (the peak at $2\Theta \approx 23.75°$), which is good for achieving efficient solar cells based on CdTe thin films.

Based on the values of FWHM peaks and the Miller indices (hkl) obtained by the Gaussian approximation method (Origin software), the structural parameters of CdTe thin films were also calculated.

The lattice constants (a, b, c) were found according to the equation [37]:

$$a = d\sqrt{h^2 + k^2 + l^2}, \tag{2}$$

where h, k, l are the Miller indices. This form of the equation applies to the thin films have the cubic crystal structure ($a = b = c$, $\alpha = \beta = \gamma = 90°$). The interplanar distance (d) was calculated through the use of the Bragg`s diffraction law [37]:

$$2d \cdot \sin\theta = n \cdot \lambda, \tag{3}$$

where θ is the Bragg angle; λ is incident CuKα radiation wavelength.

The calculated lattice parameters ($a = b = c$) and interplanar distance (d) of the investigated films are 6.48 Å and 3.74 Å, respectively, that match the theoretical

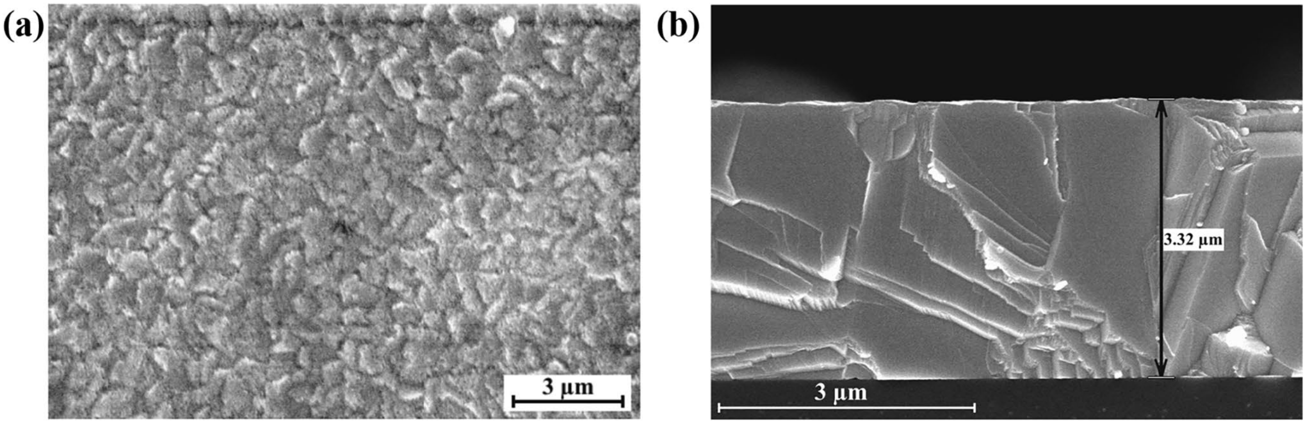

Figure 1 SEM **a** and cross-sectional images **b** of CdTe thin films

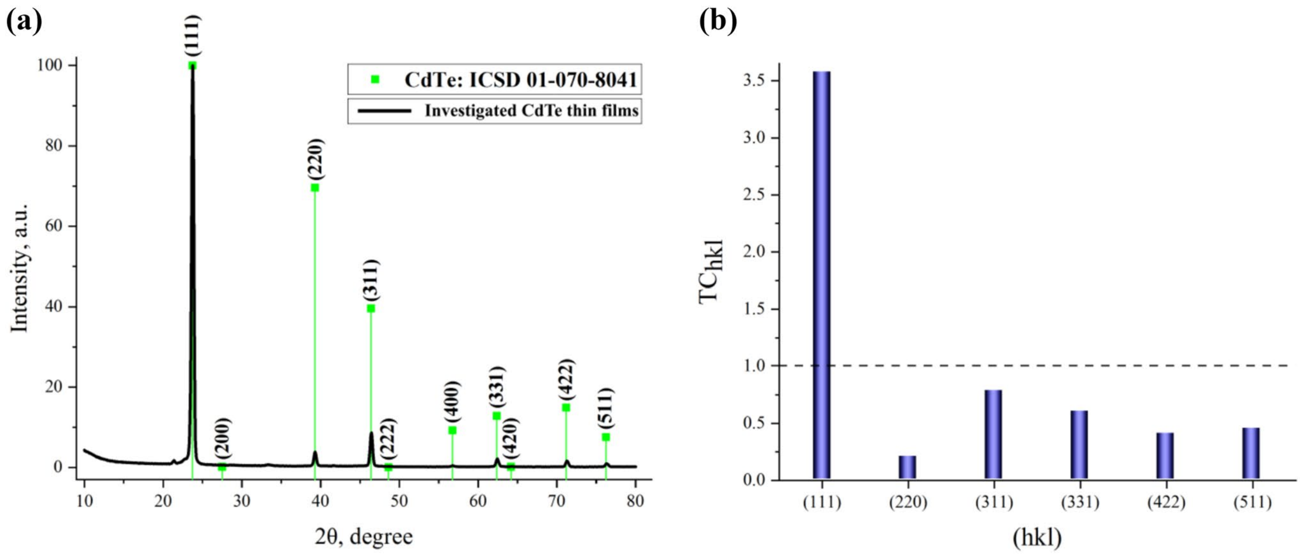

Figure 2 GIXD pattern **a** and the texture coefficient **b** of CdTe thin films

values of the CdTe cubic structure (according to ICSD Card No.: 01-070-804: $a = b = c = 6.483$ Å and $d = 3.74$ Å).

The coherent scattering region size (L) and the lattice deformation (ε) were counted by the Williamson–Hall method with the uniform deformation model (UDM) represented as equation [38–41]

$$\beta \cos\theta = \frac{K\lambda}{L} + 4\varepsilon \sin\theta, \tag{4}$$

where K is shape factor (0.94).

The dislocation density (δ) was calculated according to the well-known Williamson–Smallman ratio [37]:

$$\delta = \frac{1}{L^2}, \tag{5}$$

The obtained value of the coherent scattering region (L) is 64 nm, of the lattice deformation (ε) is ~ $3{\cdot}10^{-4}$, and of the dislocation density (δ) is 2.4×10^{14} lines/m^2 [35].

The attributes of the most highly intense lines to the CdTe structure, the absence of intense peaks indicating the presence of secondary phases, and the obtained TC_{hkl} coefficients indicating the preferred orientation along the plane (111) of the CdTe structure allow to make a conclusion that the investigated thin films crystallize in the cubic CdTe structure.

The influence of microstructure on the functional properties of polycrystalline films is a critical consideration. The SEM and GIXD analysis revealed a grain size of approximately 1 μm and a coherent scattering region size of 64 nm, indicating the presence of subgrain structure or defects within the larger grains. For photovoltaic applications, grain boundaries in CdTe are known to act as recombination centers for charge carriers, potentially limiting device efficiency [7]. However, the low lattice deformation (ε ~ $3{\cdot}10^{-4}$) suggests a relatively relaxed film with minimal residual strain. While size-induced effects like surface compression can alter the band gap in nanocrystalline materials, the micron-scale grain size observed here makes such effects negligible for the bulk properties probed by Raman spectroscopy. Therefore, the primary impact of the microstructure in our films is likely on electronic transport properties, while the measured phonon anharmonicity reflects the intrinsic properties of the CdTe lattice within the grains.

Raman spectroscopy of CdTe thin films

The structure of CdTe thin films was also studied by Raman spectroscopy. To find the Raman bands, the approximation of the Raman spectra (at room temperature in air) by the Lorentz function was used (Fig. 3). The results are presented in Table 1.

Four pronounced peaks (98, 124, 141, 165 cm^{-1}) and several mild ones (70, 82, 185, 273, 327 cm^{-1}) are observed in the Raman spectra of CdTe. The Raman peak at 165 cm^{-1} refers to the fundamental longitudinal optic (LO) phonon mode of CdTe [18, 35, 42–44]. The strongest feature observed at 124 cm^{-1} relates

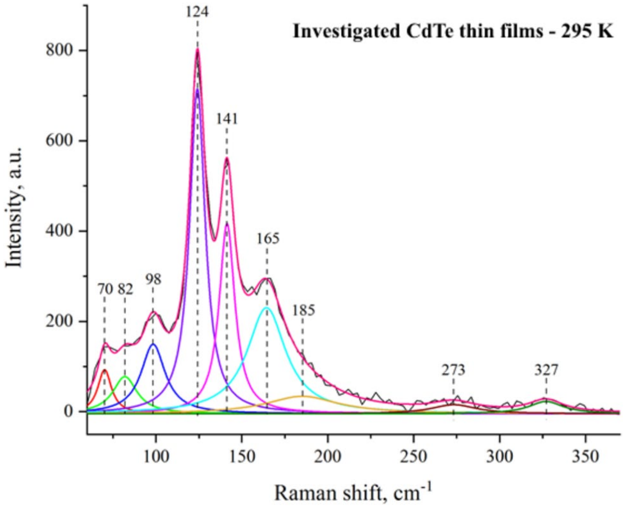

Figure 3 Raman spectra of CdTe thin films approximated by the Lorentz function

to the phonon with A_1 symmetry, while the 98 cm^{-1} feature originates from phonons with an E symmetry in the trigonal Te [42, 44–48]. The peak at 141 cm^{-1} is likely a superposition of the E mode of Te and the TO mode of CdTe [35, 43, 48, 49]. The peak located at 273 cm^{-1} is attributed to the second order harmonic of the A and E mode of Te [42, 44]. The presence of Te on the surface of CdTe films was discussed in [49–51]. The modes observed at 327 cm^{-1} and 185 cm^{-1} correspond to 2LO and 2LO-TO modes of CdTe, respectively [18, 35]. On the other hand, the Raman spectra of the oxides TeO_2, Te_2O_5, Te_4O_9, CdO are also characterized by peaks in the region of small shifts (60–200 cm^{-1}), but they are also characterized by the presence of comparable intensity lines in the range 400–850 cm^{-1}, which are not observed in our spectra, so we can talk about the absence oxide phases, which is in agreement with the results of GIXD [42, 43, 52–56].

To investigate the temperature dependence of the Raman shift of peaks position in CdTe thin films, the corresponding Raman spectra were obtained as shown in Fig. 4. The temperature changed from 295 to 40 K.

As mentioned above, the temperature dependencies of the Raman spectra of CdTe were measured in a thermostatic cell under ~ 5×10^{-4} Pa vacuum conditions. In this case, the laser radiation was focused by a long-focus 20 × lens (aperture of 0.4) into a spot with a diameter of ~ 1.6 µm. Laser power was increased to 1.6 mW to improve the signal-to-noise ratio, while the power was selected so that the peak positions (124, 141, 165 cm^{-1}) coincided with the values in the Raman spectra measured at 295 K in air (100 × (aperture 0.95), laser power 0.2 mW), effectively allowing to consider heat dissipation to be quick. As can be seen from a comparison of Figs. 3 and 4, the Raman spectrum of CdTe at room temperature in vacuum shows the intensity of 124 cm^{-1} peak has decreased, and the peak at 98 cm^{-1} is actually not recorded. This can be explained as follows: when using a 100 × lens, the surface of CdTe film makes a larger contribution to the Raman spectrum,

Table 1 The Raman bands of CdTe thin films (T = 295 K) (vw: very weak, w: weak, m: medium, s: strong and vs: very strong).

Experimental data				Literature data [18, 35, 42–56]					
Investigated CdTe thin films				CdTe	Te	TeO_2	Te_2O_5	Te_4O_9	CdO
in air		in vacuum							
PC (cm^{-1})	FWHM (cm^{-1})	PC (cm^{-1})	FWHM (cm^{-1})	PC (cm^{-1})					
70_{vw}	10	–	–	–	–	62/66	72	71	–
82_{vw}	17	–	–	–	–	–	–	77	–
98_{vw}	17	104_{m}	33	–	92	–	98	–	–
124_{vs}	11	126_{vs}	18	–	120/127	–	–	–	–
141_{m}	11	141_{vs}	13	140–142 (TO)	140/142	140	141	–	–
165_{w}	27	167_{s}	14	163–167 (LO)	–	–	–	164	–
185_{vw}	51	184_{w}	21	186 (2LO-TO)	–	184	185/187	185	–
273_{vw}	32	269_{vw}	20	264/270 (the first overtone of TO)	270	276	268/276	274	265
327_{vw}	24	331_{vw}	19	328–330 (2LO)	–	333	–	–	322

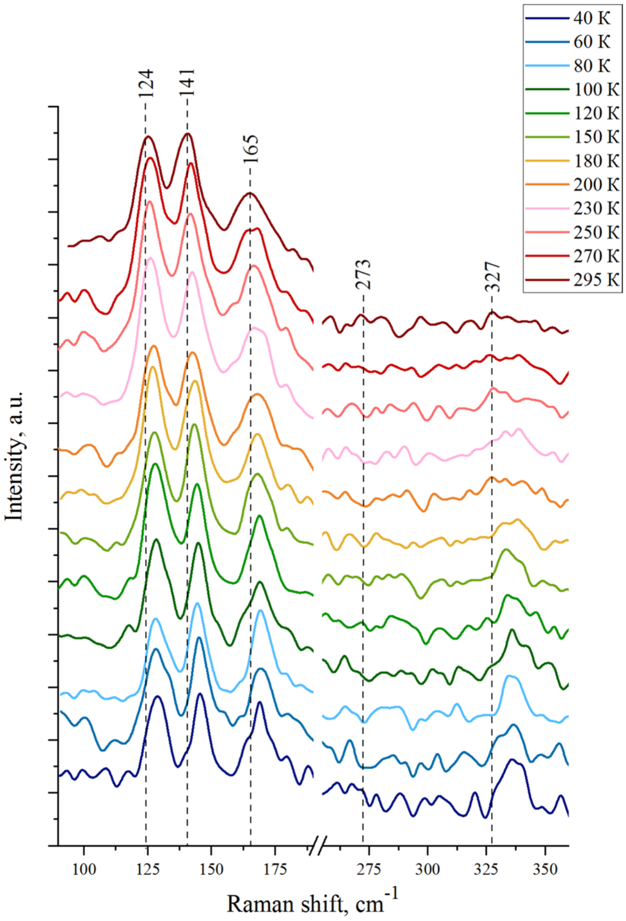

Figure 4 The temperature dependence of the Raman spectra for CdTe thin films

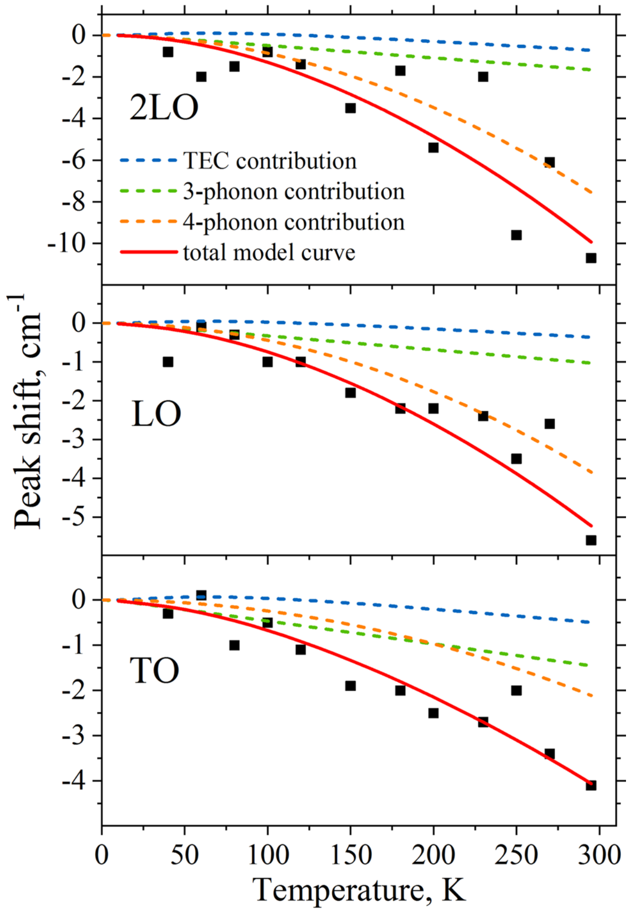

Figure 5 Relative position temperature shifts obtained for TO, LO and 2LO Raman modes of CdTe thin films, as well as the utilized model approximation. The contributions of thermal expansion, 3- and 4-phonon scattering are plotted separately

while when using a 20 × lens, the contribution of the surface to the Raman spectrum decreases due to the greater depth of field, which leads to a decrease in the intensity of peaks associated with Te, and indirectly indicates enrichment of film surfaces with it. Besides, the decrease in the intensity of 124 cm^{-1} peak can be related to the removal of chemisorbed oxygen during the pumping process.

When the temperature decreases to 40 K, a shift of TO and LO modes of CdTe (~ 141 cm^{-1}, ~ 165 cm^{-1}) by approximately 5 cm^{-1} to the region of higher values is observed. The position of 2LO CdTe mode (327 cm^{-1}) shifted by about 10 cm^{-1}.

Since no mechanical strain is expected to emerge within this experiment, the relative position temperature shift $\Delta\omega(T)$ for a Raman mode can be described through distinguishing the volumetric thermal expansion contribution $\Delta\omega_V$ and the anharmonic multiphonon interaction contribution $\Delta\omega_{ph\text{-}ph}$ [16, 19, 20]:

$$\Delta\omega_i = \Delta\omega^i_V(T) + \Delta\omega^i_{ph-ph}(T), \tag{6}$$

The relative position shifts obtained for TO, LO and 2LO modes are presented in Fig. 5. The linear approximation is often used to fit this type of data, as for example in [57, 58]; however, clear nonlinearity is evident from Fig. 5, implying the necessity of a more advanced approach. For comparative purposes, linear approximations are presented in Appendix A.

The thermal expansion contribution can be considered directly through the mode-specific Grüneisen parameter γ_i by integrating the volume thermal expansion coefficient temperature dependence $\beta(T)$. Since it was found that introducing $\omega_i(T) \approx \omega^i{}_0$ assumption does not affect the $\Delta\omega^{i}{}_{V}$ calculation results notably [16], we can describe this term as

$$\Delta\omega^{i}_{V}(T) = -\gamma_i \int_0^T \beta\omega_i dT' \approx -\omega^{i}_{0}\gamma_i \int_0^T \beta dT', \quad (7)$$

where γ_i is of 1.61 for transverse phonons of 1.01 for longitudinal phonons [16, 59]. The thermal expansion was integrated using its temperature dependencies from [60, 61].

The multiphonon interaction term can be obtained using the extended Klemens model [13–15], which allows one to consider 3-phonon and 4-phonon scattering separately:

$$\Delta\omega^{i}_{ph-ph}(T) = A^{i}_{3}\left[1+\frac{2}{\exp\left(\frac{\hbar\omega^{i}_{0}}{2kT}\right)-1}\right] + B^{i}_{4}\left[1+\frac{3}{\exp\left(\frac{\hbar\omega^{i}_{0}}{3kT}\right)-1}+\frac{3}{\left(\exp\left(\frac{\hbar\omega^{i}_{0}}{3kT}\right)-1\right)^{2}}\right], \quad (8)$$

where $A_3{}^{i}$ and $B_4{}^{i}$ are the 3- and 4-phonon anharmonic constants, respectively; $\hbar$ and k are the Planck and Boltzmann constants.

The anharmonic constants were calculated as approximation parameters by fitting the experimental shifts using expression (6), where terms (7) and (8) were directly substituted. The results of a model fit are presented in Table 2 and in Fig. 5 as dashed and solid lines; the separate plotting of thermal expansion, 3-phonon and 4-phonon contributions allows one to compare their influence separately. The dependencies are in general agreement with theoretical phonon energy analysis [12], with the experimental results published by other authors [16–18], as well as with those for CdS [19]. As seen, the model corresponds to the experiment reasonably well, with the thermal expansion contribution being the smallest although non-negligible one. Its overall value for TO, LO and 2LO modes is within the range from −0.7 to 0.1 cm^{-1}, reaching maximum at 62.7 K and becoming negative at 120.1 K (these temperature points are similar for all three modes). The 3-phonon scattering is the dominating mechanism for TO, LO and 2LO modes from a temperature close to zero until 200.4, 70.9 and 43.8 K, respectively. As the temperature continues to rise, the 4-phonon interactions start to induce major contributions to the phonon energy shift, reaching −2.1, −3.8 and −7.6 cm^{-1} at a room temperature for TO, LO and 2LO modes, respectively, significantly exceeding the −1.5, −1.0 and −1.7 cm^{-1} for the 3-phonon interaction case. This interestingly adds to the results from [16], where the 4-phonon contribution had to be neglected to ensure convergence, thus leading to the 3-phonon process domination; at the same time, this is in agreement with [62, 63], where the significance of 4-phonon processes was demonstrated.

As seen from Table 2, the $A_3{}^{TO}$ and $A_3{}^{LO}$ constants have relatively close values, while $B_4{}^{TO}$ and $B_4{}^{LO}$ differ more significantly, indicating the 4-phonon processes introduce the main difference between transverse and longitudinal anharmonicity in this case. At the same time, constants for 2LO are an order of magnitude larger, implying the phonon–phonon interactions drastically increased in this case. The overall errors are in the ~ 20–30% range, except for that of $B_4{}^{2LO}$, where the larger error of ~ 35% can be found. These are related to the scattered experimental point distribution. It is interesting to note that $A_3{}^{LO}$ and $B_4{}^{LO}$ values are very close to those obtained in [19] for CdS.

Beside the position temperature dependence, the Raman mode linewidth is also indicative of anharmonic phonon lifetime [13–15]. Thermal expansion does not contribute to the FWHM, which is basically defined by

Table 2 Anharmonic constants and extrapolated values near absolute zero temperature for peak position $A_3{}^{i}$, $B_4{}^{i}$, $\omega_0{}^{i}$ and width $C_3{}^{i}$, $D_4{}^{i}$, $\Gamma_0{}^{i}$ for TO, LO and 2LO Raman peaks of CdTe thin films

Peak	$\omega_0{}^{i}$, cm^{-1}	$A_3{}^{i}$, cm^{-1}	$B_4{}^{i}$, cm^{-1}	$\Gamma_0{}^{i}$, cm^{-1}	$C_3{}^{i}$, cm^{-1}	$D_4{}^{i}$, cm^{-1}
TO	145.7	$-(4.23 \pm 0.98)\cdot10^{-2}$	$-(1.01 \pm 0.28)\cdot10^{-3}$	6.4	$(2.29 \pm 0.47)\cdot10^{-3}$	$(4.73 \pm 1.51)\cdot10^{-6}$
LO	169.7	$-(3.50 \pm 0.83)\cdot10^{-2}$	$-(2.47 \pm 0.66)\cdot10^{-3}$	7.5	$(2.17 \pm 0.54)\cdot10^{-3}$	$(2.05 \pm 0.64)\cdot10^{-5}$
2LO	337.9	$-(1.16 \pm 0.29)\cdot10^{-1}$	$-(1.92 \pm 0.67)\cdot10^{-2}$	7.7	$(2.53 \pm 0.76)\cdot10^{-3}$	$(2.13 \pm 0.79)\cdot10^{-5}$

crystal translation symmetry breakdown due to defects Γ_0 and anharmonic phonon decay $\Gamma_{ph\text{-}ph}$ [13–15]:

$$\Gamma_i(\mathrm{T}) = \Gamma^i_0(T) + \Gamma^i_{ph-ph}(T), \tag{9}$$

where the first term can be considered constant in the low-temperature range, while the second one is temperature-dependent. Thus, we can use the following expression for FWHM temperature shift [13, 15]:

$$\Delta\Gamma^i = \Delta\Gamma^i_{(ph-ph)}(T) = C^i_3\left[1+\frac{2}{\exp\left(\frac{\hbar\Gamma^i_0}{2kT}\right)-1}\right] + D^i_4\left[1+\frac{3}{\exp\left(\frac{\hbar\Gamma^i_0}{3kT}\right)-1}+\frac{3}{\left(\exp\left(\frac{\hbar\Gamma^i_0}{3kT}\right)-1\right)^2}\right], \tag{10}$$

The resultant fit is given in Table 2 numerically and in Fig. 6 visually in a manner similar to the peak position fit results. As seen, the model curves correspond to the experiment quite well again, showing the overall dominance of 4-phonon processes as well. The 3-phonon process contribution is larger in the low-temperature range until 104.4, 25.5 and 30.2 K, respectively, for TO, LO and 2LO modes. The corresponding total room temperature contributions are of 1.8, 1.5 and 1.7 cm^{-1} in the case of 3-phonon scattering and of 5.2, 16.3 and 16.5 cm^{-1} for the 4-phonon interactions, respectively.

As seen from Table 2, the $C_3{}^i$ constants can be considered similar within the error for all three modes, as well as are close the values for both $C_3{}^i$ and $D_4{}^i$ for LO and 2LO. At the same time, the $D_4{}^i$ values increase approximately 4 to 5 times as we move from longitudinal to transverse phonons, which seems reasonable for T_d symmetry of zinc blende structure [64, 65]. It should be noted that the $D_4{}^i$ constants show the largest errors of up to ~ 37%, making these values somewhat less defining.

Summarizing the data discussion, the analyzed nonlinear peak shift is caused by a change in the rigidity of the crystal lattice with a change in the interatomic distances with the temperature; freezing of phonon modes which leads to the dominance of 3-phonon processes at low temperatures (below 30–200 K, depending on the mode); and increase in multiparticle interactions at high temperatures, which contribute up to 70% to the mode energy shift. The dominance of 4-phonon processes at higher temperatures directly affects the thermal conductivity, which inversely relates to the phonon decay [66], as well as the electron–phonon scattering rate. The obtained $B_4{}^i$ constants (Table 2) allow refining the transport models in the framework of performance increase challenge for CdTe devices [7].

The observed transition from 3- to 4-phonon dominance at higher temperatures is consistent with models for 2D materials, where anharmonicity is enhanced due to lower dimension of the systems [67]. This confirms the influence of film morphology (grain size ~ 1 μm) on phonon dynamics.

In general, our results demonstrate the significance of taking into account the 4-phonon interactions while analyzing the vibrational properties of CdTe.

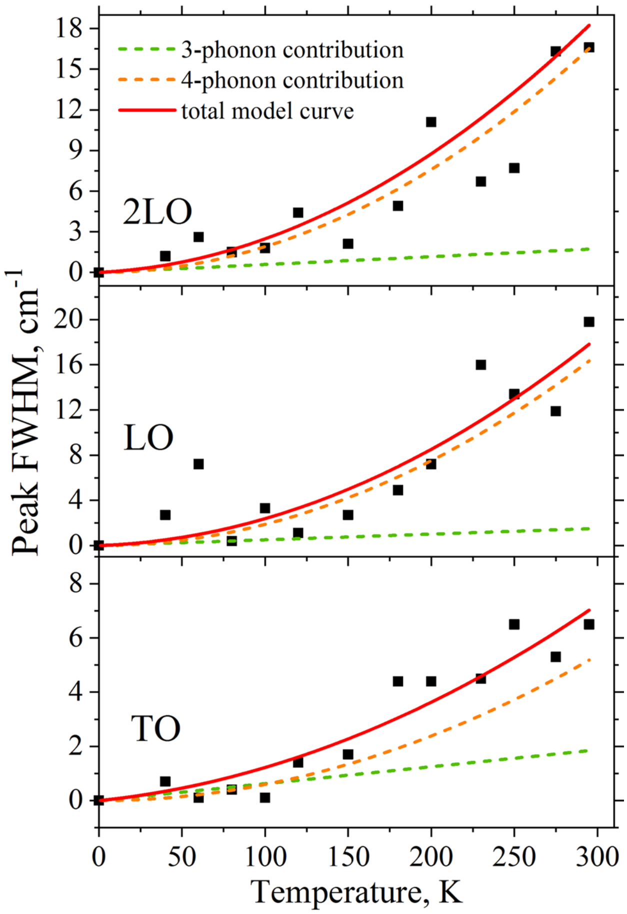

Figure 6 Relative FWHM temperature shifts obtained for TO, LO and 2LO Raman modes of CdTe thin films, as well as the utilized model approximation. The contributions of 3- and 4-phonon scattering are plotted separately

The transition from 3-phonon to 4-phonon dominance around 200 K for the TO mode falls close to the lower border of typical photovoltaic device operating range, while for other modes, this range is dominated by the 4-phonon interactions. This underscores the importance of accounting for multiphonon scattering when modeling the efficiency of CdTe-based solar cells operating under real-world conditions. Moreover, the anharmonic phonon decay affects thermal conductivity, electric and thermoelectric properties, both through influencing the electron–phonon scattering rate and leading to optical phonons decaying into acoustic ones, which will directly affect the conduction of heat [21, 22, 66]. This additionally underlines the importance of studying phonon anharmonicity in CdTe for the precise and efficient design of photovoltaic and optoelectronic devices.

Conclusion

In this work, we studied structural and phonon properties of CdTe thin films prepared by the discrete vacuum thermal evaporation using X-ray energy-dispersive spectroscopy, scanning electron microscopy, grazing incidence X-ray diffraction and temperature-dependent Raman spectroscopy. Structural studies indicated the absence of secondary phases and crystallization of the films in the main phase of CdTe with the cubic structure and with the lattice parameters close to literature data. It was also found that CdTe thin films have the composition close to stoichiometry (Cd/Te ratio was of about 1.1) and continuous surface with the grain sizes of ~ 1 μm and larger. The thickness of the films was of 3.3 μm. These results indicate that CdTe thin films obtained by the discrete vacuum thermal evaporation are fit as the base layers for high-efficiency solar cells.

Raman spectroscopy under temperatures decreasing from 295 to 40 K showed the pronounced, clearly nonlinear, peak position upshift by 4.1 cm^{-1} for TO mode of CdTe (at ~ 141 cm^{-1}), by 5.6 cm^{-1} for the LO mode (~ 165 cm^{-1}) and by 10.7 cm^{-1} for the 2LO mode (~ 327 cm^{-1}). Using the extended Klemens model and having calculated the thermal expansion contribution, the anharmonic constants were determined. We found that 3-phonon scattering was the dominant reason for the position shift of TO, LO and 2LO modes from a temperature close to zero until 200.4, 70.9 and 43.8 K, respectively. With the further temperature increase, the 4-phonon interactions start to introduce the main contribution to the phonon energy shift. The influence of thermal expansion was small but non-negligible, with the absolute values of up to 0.7 cm^{-1}. The corresponding temperature-dependent changes in the phonon decay (linewidth) of 6.5, 19.8 and 16.6 cm^{-1} for TO, LO and 2LO modes, respectively, were also dominated by 3-phonon processes in the low temperature range until 104.4, 25.5, and 30.2 K, whereupon the contribution of 4-phonon scattering became the main process responsible for the energy shift. These results can be used to take into account anharmonic phonon–phonon scattering during design of CdTe-based photovoltaic and optoelectronic devices.

Author contributions

M.S. Tivanov contributed to conceptualization, data curation, investigation, writing—original draft, writing—review and editing, and supervision. A.A. Zgliui contributed to data curation, investigation, visualization, writing—original draft, and writing—review and editing. V.A. Gevorgyan contributed to conceptualization, data curation, investigation, writing—original draft, and writing—review and editing. O.V. Korolik contributed to methodology, investigation, data curation, and writing—review and editing. E.A. Kolesov contributed to validation, conceptualization, data curation, investigation, writing—original draft, and writing—review and editing. K.P.Haroyan performed formal analysis, writing—original draft, and writing—review and editing. D.V.Zhyhulin performed investigation. V.F. Gremenok performed writing—review and editing.

Funding

This work was supported by the State Research Program of the Republic of Belarus “Material Science, New Materials and Technologies” (Task No. 1.4.2).

Data availability

Raw data from this study are available upon request to the corresponding author.

Declarations

Competing interests The authors declare no conflicts of interest or competing interests associated with this publication.

Appendix A

Since the linear approximation is often used to describe Raman peak position and width temperature dependence, we present the results of such fit below. Due to the pronounced nonlinearity of the dependence, a satisfactory agreement between the approximation curve and the experiment was achieved only in the case of two approximations in two temperature ranges: one from 40 to 150 K and the other from 180 to 295 K. The results are presented in Fig. 7.

The linear approximation of the obtained plots can be described by an equation of Grüneisen model of the following form [57, 58]:

$$\omega(T) = \omega_0 + \chi_{RS} T, \tag{11}$$

where ω_0 is the extrapolated phonon frequency near the absolute zero, and χ_{RS} is a linear shift temperature coefficient.

A similar formula in the form [68]

$$\Gamma(T) = \Gamma_0 + \chi_{FWHM} T, \tag{12}$$

was used to find FWHM at T = 0 K (Γ_0) and the corresponding temperature coefficient χ_{FWHM}.

The estimated values of ω_0 and Γ_0 near the absolute zero, as well as χ_{RS} and χ_{FWHM} temperature coefficients for the main CdTe Raman bands, are shown in Table 3.3.

The negative temperature coefficient χ_{RS} accounts for the observed shift of the Raman peak position toward shorter wavelengths [68]. This sign generally indicates that these shift changes are the result of thermal expansion or anharmonicity contributions [69, 70].

As seen from Fig. 7 and Table 3, the linear approximation is applicable only in narrow low-temperature ranges, as evidenced by very different visual slope and calculated parameters of the approximation lines. This complicates the choice of the temperature coefficients capable of describing the temperature dependences of the position and FWHM of the main Raman bands in their entirety, as well as raises doubts about the general possibility of a comprehensive temperature dependence description using this method. Still, the parameters presented in Table 3 may be useful in terms of comparison and reference use.

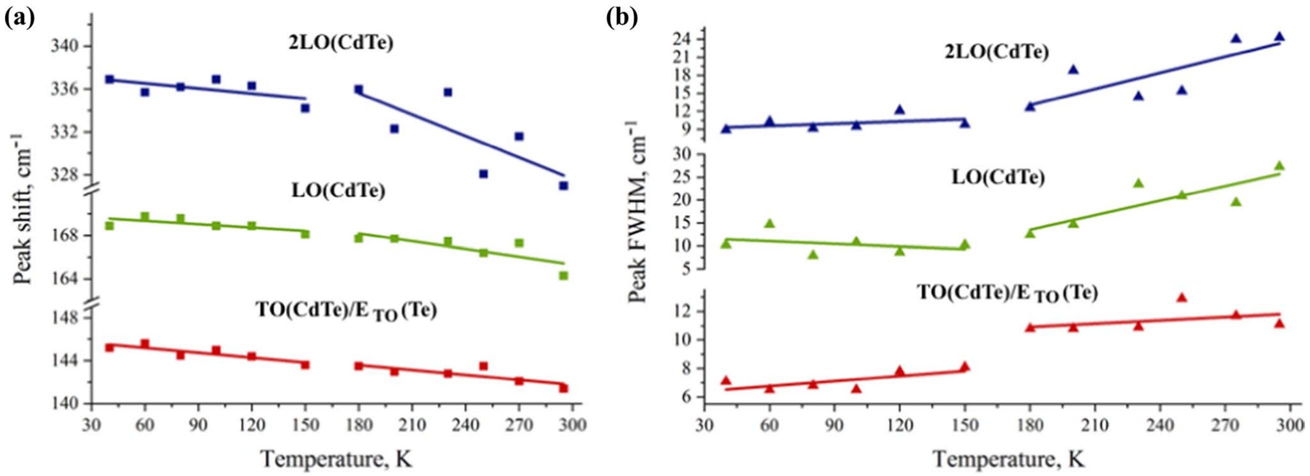

Figure 7 Temperature dependence of **a** position and **b** FWHM of TO(CdTe)/E_{TO}(Te), LO, 2LO Raman modes for CdTe thin film, as well as the corresponding linear fits

Table 3 The calculated ω_0, Γ_0, χ_{RS} and χ_{FWHM} values for CdTe thin films

T, K	Peak	ω_0, cm^{-1}	χ_{RS}, cm^{-1}/K	Γ_0, cm^{-1}	χ_{FWHM}, cm^{-1}/K
40–150	TO(CdTe)/E_{TO}(Te)	146.1	−0.015	6.0	0.012
	LO	170.0	−0.010	12.2	−0.019
	2LO	337.5	−0.016	8.8	0.012
180–295	TO(CdTe)/E_{TO}(Te)	146.4	−0.015	9.5	0.008
	LO	172.5	−0.024	−5.5	0.106
	2LO	347.6	−0.067	−3.1	0.089

References

[1] Bibin J, Varadharajaperumal S (2022) Comprehensive Review on CdTe crystals: Growth, Properties, and Photovoltaic Application. Turk J Elec Eng & Comp Sci 2:180. https://doi.org/10.5152/tepes.2022.22016

[2] Kapadnis RS, Bansode SB, Supekar AT, Bhujbal PK et al (2020) Cadmium Telluride/cadmium sulfide thin films solar cells: a review. ES Energy Environ. https://doi.org/10.30919/esee8c706

[3] Gu P, Zhu X, Li J, Wu H, Yang D (2018) Influence of sputtering power on structural, optical and electrical properties of CdTe thin films prepared by DC magnetron sputtering. J Mater Sci Mater Electron 29:14635. https://doi.org/10.1007/s10854-018-9599-6

[4] Orletskyi I, Ilashchuk M, Maistruk E, Koziarskyi I, Koziarskyi D (2022) Electrical properties of the n-NiS$_2$/n-CdTe isotype heterojunction fabricated by spray pyrolysis. Acta Phys Pol A 142:615. https://doi.org/10.12693/APhysPolA.142.615

[5] Romeo A, Artegiani E (2021) CdTe-based thin film solar cells: past, present and future. Energies 14:1684. https://doi.org/10.3390/en14061684

[6] Fthenakis V, Athias C, Blumenthal A, Kulur A et al (2020) Sustainability evaluation of CdTe PV: an update. Renew Sustain Energy Rev 123:109776. https://doi.org/10.1016/j.rser.2020.109776

[7] Scarpulla MA, McCandless B, Phillips AB, Yan Y et al (2023) CdTe-based thin film photovoltaics: recent advances, current challenges and future prospects. Sol Energy Mater Sol Cells 255:112289. https://doi.org/10.1016/j.solmat.2023.112289

[8] Krasikov D, Sankin I (2017) Defect interactions and the role of complexes in the CdTe solar cell absorber. J Mater Chem A 5:3503. https://doi.org/10.1039/c6ta09155e

[9] Bosio A, Pasini S, Romeo N (2020) The history of photovoltaics with emphasis on CdTe solar cells and modules. Coatings 10:344. https://doi.org/10.3390/coatings10040344

[10] Takeuchi H, Yokogawa R, Takahashi K, Komori K et al (2020) Thermal conductivity characteristics in polycrystalline silicon with different average sizes of grain and nanostructures in the grains by UV Raman spectroscopy. Jpn J Appl Phys 59:075501. https://doi.org/10.35848/1347-4065/ab9624

[11] Klein FW, Huntzinger J-R, Astié V, Voiry D et al (2024) Determining by raman spectroscopy the average thickness and N-layer-specific surface coverages of MoS$_2$ thin films with domains much smaller than the laser spot size. Beilstein J Nanotechnol 15:279. https://doi.org/10.3762/bjnano.15.26

[12] Akil NA, Guo S-D (2023) Lattice thermal transport of BAs, CdSe, CdTe, and GaAs: a first principles study. J Electron Mater 52:3401. https://doi.org/10.1007/s11664-023-10305-0

[13] Debernardi A, Baroni S, Molinari E (1995) Anharmonic phonon lifetimes in semiconductors from density-functional perturbation theory. Phys Rev Lett 75:1819. https://doi.org/10.1103/PhysRevLett.75.1819

[14] Cowley RA (1968) Anharmonic crystals. Rep Prog Phys 31:123. https://doi.org/10.1088/0034-4885/31/1/303

[15] Balkanski M, Wallis RF, Haro E (1983) Anharmonic effects in light scattering due to optical phonons in silicon. Phys Rev B 28:1928. https://doi.org/10.1103/PhysRevB.28.1928

[16] Stergiou VC, Kontos AG, Raptis YS (2008) Anharmonic effects and Faust-Henry coefficient of CdTe in the vicinity of the energy gap. Phys Rev B 77:235201. https://doi.org/10.1103/PhysRevB.77.235201

[17] Li J-C, Li L-S, Sun W (2020) Temperature dependence on dielectric properties of CdTe and ZnTe using first-principles method and experimental data. Procedia Computer Science 174:673. https://doi.org/10.1016/j.procs.2020.06.141

[18] Li X, Liu D, Wang D (2018) Anharmonic phonon decay in polycrystalline CdTe thin film. Appl Phys Lett 112:252105. https://doi.org/10.1063/1.5033987

[19] Freitas Neto ES, Dantas NO, da Silva SW, Morais PC et al (2012) Temperature-dependent raman study of thermal parameters in CdS quantum dots. Nanotechnology

23:125701. https://doi.org/10.1088/0957-4484/23/12/125701

[20] Kolesov EA, Tivanov MS, Korolik OV, Kapitanova OO et al (2019) Phonon anharmonicities in supported graphene. Carbon 141:190. https://doi.org/10.1016/j.carbon.2018.09.020

[21] Liu MS, Bursill LA, Prawer S (2000) Temperature dependence of the first-order Raman phonon line of diamond. Phys Rev B 61:3391. https://doi.org/10.1103/PhysRevB.61.3391

[22] Yadav D, Pauly F, Trushin M (2021) Charge-carrier thermalization in bulk and monolayer CdTe from first principles. Phys Rev B 103:125113. https://doi.org/10.1103/PhysRevB.103.125113

[23] Chang H, Feng S, Qiu X, Meng H et al (2020) Implementation of the toroidal absorption cell with multi-layer patterns by a single ring surface. Opt Lett 45:5897. https://doi.org/10.1364/OL.404198

[24] Tishkevich DI, Grabchikov SS, Lastovskii SB, Trukhanov SV et al (2018) Correlation of the synthesis conditions and microstructure for Bi-based electron shields production. J Alloys Compd 749:1036. https://doi.org/10.1016/j.jallcom.2018.03.288

[25] Al-Ghamdi AA, Khan SA, Nagat A, Abd El-Sadek MS (2010) Synthesis and optical characterization of nanocrystalline CdTe thin films. Opt Laser Technol 42:1181. https://doi.org/10.1016/j.optlastec.2010.03.007

[26] Petrus R, Ilchuk H, Kashuba A, Semkiv I, Zmiiovska E (2020) Optical properties of CdTe thin films obtained by the method of high-frequency magnetron sputtering. Funct Mater. https://doi.org/10.15407/fm27.02.342

[27] Arce-Plaza A, Sánchez-Rodriguez F, Courel-Piedrahita M, Vigil Galán O et al (2019) CdTe thin films: deposition techniques and applications. Coat Thin-Film Tech. https://doi.org/10.5772/intechopen.79578

[28] Gevorgyan VA, Hakhoyan LA, Mangasaryan NR, Gladyshev PP (2016) Substrate temperature and annealing effects on the structural and optical properties of nano-Cds films deposited by vacuum flash evaporation technique. Front Nanosci Nanotech. https://doi.org/10.15761/FNN.1000114

[29] Gevorgyan VA, Mangasaryan NR, Gremenok VF, Tivanov MS et al (2023) Morphology and structure of $CdCl_2$-containing CdTe films deposited by discrete vacuum thermal evaporation. Vacuum 214:112248. https://doi.org/10.1016/j.vacuum.2023.112248

[30] Shpylka DO, Ovsiienko IV, Len TA, Matzui LY et al (2022) The features of the magnetoresistance of carbon nanotubes modified with Fe. Ceram Int 48:19789. https://doi.org/10.1016/j.ceramint.2022.03.253

[31] Lin S, Li X, Zhang S, Wang P et al (2015) Graphene/CdTe heterostructure solar cell and its enhancement with photo-induced doping. Appl Phys Lett 107:191106. https://doi.org/10.1063/1.4935426

[32] Camacho RE, Morgan AR, Flores MC, McLeod TA et al (2007) Carbon nanotube arrays for photovoltaic applications. JOM 59:39. https://doi.org/10.1007/s11837-007-0037-0

[33] Hall RS, Lamb D, Irvine SJC (2021) Back contacts materials used in thin film CdTe solar cells – a review. Energy Sci Eng 9:606. https://doi.org/10.1002/ese3.843

[34] Leon IM, Reinhard G (1970) Handbook of Thin Film Technology. McGraw-Hill

[35] Tivanov MS, Gevorgyan VA, Zgliui AA, Haroyan KP et al (2025) Structure and optical properties of CdTe thin films obtained via discrete vacuum thermal evaporation. J Mater Sci Mater Electron 36:699. https://doi.org/10.1007/s10854-025-14769-0

[36] Pandey A, Dala S, Dutta S, Dixit A (2021) Structural characterization of polycrystalline thin films by X-ray diffraction techniques. J Mater Sci: Mater Electron. https://doi.org/10.1007/s10854-020-04998-w

[37] Salunkhe P, A.V. MA, Kekuda D (2020) Investigation on tailoring physical properties of Nickel oxide thin films grown by dc magnetron sputtering. Mater Res Express 7:016427. https://doi.org/10.1088/2053-1591/ab69c5

[38] Birkholz M (2006) Thin film analysis by X-ray scattering. J Appl Cryst 39:925. https://doi.org/10.1107/S0021889806034698

[39] Patel K, Patel A, Jethwa VP, Patel H, Solanki GK (2024) X-ray diffraction analysis of orthorhombic SnSe nanoparticles by Williamson-Hall, Halder-Wagner and Size-Strain plot methods. Chemical Physics Impact 8:100547. https://doi.org/10.1016/j.chphi.2024.100547

[40] Mote V, Purushotham Y, Dole B (2012) Williamson-hall analysis in estimation of lattice strain in nanometer-sized ZnO particles. J Theor Appl Phys 6:6. https://doi.org/10.1186/2251-7235-6-6

[41] Saritha K, Rasool S, Reddy KTR, Saad AM et al (2019) Substrate temperature dependent physical properties of $SnS_{1-x}Se_x$ thin films. Appl Phys A 125:704. https://doi.org/10.1007/s00339-019-3003-0

[42] Quiñones-Galván JG, Camps E, Campos-González E, Hernández-Hernández A et al (2015) Influence of plasma parameters and substrate temperature on the structural and optical properties of CdTe thin films deposited on glass by laser ablation. J Appl Phys 118:125304. https://doi.org/10.1063/1.4931677

[43] Gunjal SD, Khollam YB, Jadkar SR, Shripathi T et al (2014) Spray pyrolysis deposition of p-CdTe films: structural, optical and electrical properties. Sol Energy 106:56. https://doi.org/10.1016/j.solener.2013.11.029

[44] Zhu F, Tan S, Dhinakaran MK, Cheng J, Li H (2020) The light-driven macroscopic directional motion of a water droplet on an azobenzene–calix[4]arene modified surface. Chem Commun 56:10922. https://doi.org/10.1039/D0CE00519C

[45] Tang G, Qian Q, Wen X, Zhou G, Chen X, Sun M, Yang Z (2015) Phosphate glass-clad tellurium semiconductor core optical fibers. J Alloys Compd 633:1. https://doi.org/10.1016/j.jallcom.2015.02.007

[46] Mitric J, Paunovic N, Mitric M, Vasic B et al (2018) Surface optical phonon – plasmon interaction in nanodimensional CdTe thin films. Physica E 104:64. https://doi.org/10.1016/j.physe.2018.07.021

[47] Du Y, Qiu G, Wang Y, Si M et al (2017) One-dimensional van der Waals material Tellurium: Raman spectroscopy under strain and magneto-transport. Nano Lett 17:3965. https://doi.org/10.1021/acs.nanolett.7b01717

[48] Pine AS, Dresselhaus G (1971) Raman spectra and lattice dynamics of tellurium. Phys Rev B 4:356. https://doi.org/10.1103/PhysRevB.4.356

[49] Amirtharaj PM, Pollak FH (1984) Raman scattering study of the properties and removal of excess Te on CdTe surfaces. Appl Phys Lett 45:789. https://doi.org/10.1063/1.95367

[50] Soares MJ, Lopes JC, Carmo MC, Neves A (2004) Micro-raman study of laser damage in CdTe. Phys Stat Sol (c) 1:278. https://doi.org/10.1002/pssc.200303931

[51] Soares J, do Carmo C (2001) Raman characterization of Te inclusions on CdTe surfaces using visible lasers. Proc SPIE 4469:57. https://doi.org/10.1117/12.447373

[52] Smirnov M, Kuznetsov V, Roginskii E, Cornette J et al (2018) Raman spectra and structural peculiarities of TeO_2–TeO_3 mixed oxides. J Phys: Condens Matter 30:475403. https://doi.org/10.1088/1361-648X/aae811

[53] Gupta N, Kaur A, Khanna A, Gonzàlez F et al (2017) Structure-property correlations in TiO_2-Bi_2O_3-B_2O_3-TeO_2 glasses. J Non-Cryst Solids 470:168. https://doi.org/10.1016/j.jnoncrysol.2017.05.021

[54] Abu Sal B, Moiseyenko V, Dergachov M, Yevchik A, Dovbeshko G (2013) Manifestation of metastable gamma-TeO2 phase in the Raman spectrum of crystals grown in synthetic opal pores. Ukr J Phys Opt 14:119. https://doi.org/10.3116/16091833/14/3/119/2013

[55] Kalampounias AG, Tsilomelekis G, Boghosian S (2015) Glass-forming ability of TeO_2 and temperature induced changes on the structure of the glassy, supercooled, and molten states. J Chem Phys 142:154503. https://doi.org/10.1063/1.4917536

[56] Srihari V, Sridharan V, Ravindran TR, Chandra S, Arora AK, Sastry VS, Sundar CS (2011) Raman scattering of cadmium oxide: in B1 phase. AIP Conf Proc 1349:845. https://doi.org/10.1063/1.3606122

[57] Irfan B, Sahoo S, Gaur APS, Ahmadi M et al (2014) Temperature dependent Raman scattering studies of three dimensional topological insulators Bi_2Se_3. J Appl Phys 115:173506. https://doi.org/10.1063/1.4871860

[58] Chen H, Ma Z, Shao Y, ur Rehman Z et al (2017) Angle-/temperature-dependence of raman scattering in layered $NbSe_3$ crystal. AIP Adv 7:095316. https://doi.org/10.1063/1.4990433

[59] Arora AK, Bartholomew DU, Peterson DL, Ramdas AK (1987) Raman-scattering study of the high-pressure phase transition in $Cd_{1-x}Mn_xTe$. Phys Rev B 35:7966. https://doi.org/10.1103/PhysRevB.35.7966

[60] Smith TF, White GK (1975) The low-temperature thermal expansion and Gruneisen parameters of some tetrahedrally bonded solids. J Phys C: Solid State Phys 8:2031. https://doi.org/10.1088/0022-3719/8/13/012

[61] Greenough RD, Palmer SB (1973) The elastic constants and thermal expansion of single-crystal CdTe. J Phys D: Appl Phys 6:587. https://doi.org/10.1088/0022-3727/6/5/315

[62] Sun W, Li L, Cai H, Li J et al (2021) Dielectric and vibrational properties of CdTe studied by first-principles and terahertz time-domain spectroscopy. Phys B: Condens Matter 602:412543. https://doi.org/10.1016/j.physb.2020.412543

[63] Huang X, Luo K, Shen Y, Yue Y, An Q (2023) Grain boundaries induce significant decrease in lattice thermal conductivity of CdTe. Energy and AI 11:100210. https://doi.org/10.1016/j.egyai.2022.100210

[64] Polit J, Kisiel A, Mycielski A, Marcelli A et al (2005) Vibrational spectra of hydrogenated CdTe. Phys Stat Sol 2:1147. https://doi.org/10.1002/pssc.200460666

[65] Xia BW, Wang R, Chen ZJ, Zhao YJ, Xu H (2019) Symmetry-protected ideal type-II Weyl phonons in CdTe. Phys Rev Lett 123:065501. https://doi.org/10.1103/PhysRevLett.123.065501

[66] Mani J, Kumar NR, Radhakrishnan R, Anbalagan G (2020) Thermoelectric properties of CdTe materials: DFT study. AIP Conf Proc 2265:030390. https://doi.org/10.1063/5.0016968

[67] Tian X, Xun R, Chang T, Yu J (2025) Distribution function of thermal ripples in h-BN, graphene and MoS_2. Phys Lett A 550:130597. https://doi.org/10.1016/j.physleta.2025.130597

[68] Stanchik AV, Tivanov MS, Tyukhov II, Juskenas R et al (2020) Temperature dependence of raman scattering in the $Cu_2ZnSnSe_4$ thin films on a Ta foil substrate. Sol Energy 201:480. https://doi.org/10.1016/j.solener.2020.03.043

[69] Late DJ (2015) Temperature dependent phonon shifts in few-layer black phosphorus. ACS Appl Mater Interfaces 7:5857. https://doi.org/10.1021/am509056b

[70] Pawbake AS, Pawar MS, Jadkar SR, Late DJ (2016) Large area chemical vapor deposition of monolayer transition metal dichalcogenides and their temperature dependent Raman spectroscopy studies. Nanoscale 8:3008. https://doi.org/10.1039/C5NR07401K